



# Anomalous Hall effect in Weyl semimetal half-Heusler compounds RPtBi (R = Gd and Nd)

Chandra Shekhar<sup>a,1</sup>, Nitesh Kumar<sup>a</sup>, V. Grinenko<sup>b,c</sup>, Sanjay Singh<sup>a</sup>, R. Sarkar<sup>b</sup>, H. Luetkens<sup>d</sup>, Shu-Chun Wu<sup>a</sup>, Yang Zhang<sup>a</sup>, Alexander C. Komarek<sup>a</sup>, Erik Kampert<sup>e</sup>, Yurii Skourski<sup>e</sup>, Jochen Wosnitza<sup>b,e</sup>, Walter Schnelle<sup>a</sup>, Alix McCollam<sup>f</sup>, Uli Zeitler<sup>f</sup>, Jürgen Kübler<sup>g</sup>, Binghai Yan<sup>a</sup>, H.-H. Klauss<sup>b</sup>, S. S. P. Parkin<sup>h,1</sup>, and C. Felser<sup>a</sup>

<sup>a</sup>Max Planck Institute for Chemical Physics of Solids, 01187 Dresden, Germany; <sup>b</sup>Institute for Solid State and Materials Physics, Faculty of Physics, Technische Universität Dresden, 01069 Dresden, Germany; <sup>c</sup>Leibniz Institute for Solid State and Materials Research Dresden, 01069 Dresden, Germany; <sup>d</sup>Laboratory for Muon Spin Spectroscopy, Paul Scherrer Institute, CH-5232 Villigen PSI, Switzerland; <sup>e</sup>Dresden High Magnetic Field Laboratory (HLD-EMFL), Helmholtz-Zentrum Dresden-Rossendorf, 01328 Dresden, Germany; <sup>f</sup>High Field Magnet Laboratory (HFML-EMFL), Radboud University, 6525 ED Nijmegen, The Netherlands; <sup>g</sup>Institute for Solid State Physics, Technische Universität Darmstadt, 64289 Darmstadt, Germany; and <sup>h</sup>Max Planck Institute of Microstructure Physics, 06120 Halle, Germany

Contributed by S. S. P. Parkin, July 23, 2018 (sent for review June 25, 2018; reviewed by Anton Burkov and Qi-kun Xue)

**Topological materials ranging from topological insulators to Weyl and Dirac semimetals form one of the most exciting current fields in condensed-matter research. Many half-Heusler compounds, RPtBi (R = rare earth), have been theoretically predicted to be topological semimetals. Among various topological attributes envisaged in RPtBi, topological surface states, chiral anomaly, and planar Hall effect have been observed experimentally. Here, we report an unusual intrinsic anomalous Hall effect (AHE) in the antiferromagnetic Heusler Weyl semimetal compounds GdPtBi and NdPtBi that is observed over a wide temperature range. In particular, GdPtBi exhibits an anomalous Hall conductivity of up to  $60 \Omega^{-1}\text{cm}^{-1}$  and an anomalous Hall angle as large as 23%. Muon spin-resonance ( $\mu\text{SR}$ ) studies of GdPtBi indicate a sharp antiferromagnetic transition ( $T_N$ ) at 9 K without any noticeable magnetic correlations above  $T_N$ . Our studies indicate that Weyl points in these half-Heuslers are induced by a magnetic field via exchange splitting of the electronic bands at or near the Fermi energy, which is the source of the chiral anomaly and the AHE.**

Heuslers | Weyl semimetal | Berry curvature | anomalous Hall conductivity | muon spin-resonance

Topological materials are a family of quantum materials that are of much interest today as they possess a range of novel phenomena which are promising for technological applications. Among these materials Weyl semimetals (WSMs) are 3D analogs of graphene, in which the conduction and valence bands disperse linearly through nodes, the Weyl points, in momentum space (1). Weyl points are singular monopoles of the Berry curvature, an intrinsic property of the electron's wave function, with “+” or “−” chirality, and, thus, always come in pairs. A hallmark of a WSM is the existence of Fermi-arc surface states (1), which connect each pair of Weyl nodes. The recent discovery of time-reversal-invariant WSMs in the TaAs-type transition-metal monpnictides (2, 3) was demonstrated via the observation of Fermi arcs (4, 5). Another hallmark of a WSM is the so-called chiral anomaly which arises from topological charge pumping between Weyl points within a pair. This gives rise to several unusual properties including a longitudinal negative magnetoresistance (nMR) (6). Furthermore, time-reversal breaking WSMs are anticipated to exhibit an anomalous Hall effect (AHE) due to the net Berry flux that is proportional to the separation of the Weyl points that have opposite chirality (7). Among the large family of WSMs, ZrTe<sub>5</sub> has recently been identified as exhibiting an AHE (8), whose magnitude is sensitive to the position of Weyl points relative to the Fermi energy ( $E_F$ ).

The extended family of Heusler compounds provides a unique platform since these materials possess a wide range of tunable structural and physical functionalities, ranging from topological insulators (9–11) to unconventional superconductivity (12). Topological surface states in several Heusler compounds have recently been observed by angle-resolved photoemission studies (13). Among the family of half-Heusler compounds, the Weyl

semimetal GdPtBi is significant because it exhibits a chiral anomaly (14), a planar Hall effect (15), a linear optical conductivity (16), and triple-point fermions (17) close to the  $E_F$ .

In this paper, we consider magnetic lanthanide half-Heusler compounds formed from RPtBi, where R is a lanthanide or Y. These compounds have an inversion asymmetric crystal structure (space group no. 216,  $F\bar{4}3m$ ). RPtBi is composed of three interpenetrating fcc lattices (Fig. 1A) so that along the [111] direction, the structure can be described as a metallic multilayer formed from successive atomic layers of rare earth, platinum, and bismuth. GdPtBi (18, 19) as well as NdPtBi (20) are antiferromagnetic (AFM) metals at low temperatures below their corresponding Néel temperatures,  $T_N = 9.0$  and 2.1 K, respectively. The Gd spins order antiferromagnetically without any canting in zero magnetic field (as evidenced from  $\mu\text{SR}$ , discussed later) and saturate into a fully spin-aligned magnetic state in high magnetic fields at low temperatures [e.g., 25 T at 1.4 K (Fig. 1B)]. This is in contrast to a previous report where the AHE between 3 and 5 T is attributed to a spin-texture Berry phase (21).

The calculated band structures of GdPtBi are given in *SI Appendix*, Fig. S1. A simplified schematic version in Fig. 1C shows how the exchange field affects the band splitting, forming Weyl points; the band inversion between the  $\Gamma_8$  and  $\Gamma_6$  bands results in a gapless semimetal with degenerate  $\Gamma_8$  bands at the  $E_F$  for all lanthanide RPtBi compounds (9). When R = Y, the compound is

## Significance

**GdPtBi and NdPtBi belong to the Heusler family of compounds and are conventional antiferromagnets below 9 and 2.1 K, respectively. We present evidence for magnetic-field-induced Weyl physics in these compounds, namely, a chiral anomaly (negative magnetoresistance) and an anomalous Hall effect (AHE) with a large anomalous Hall angle over a wide range of temperature. The AHE and chiral anomaly have a similar temperature dependence, indicating their common origin. These studies plus band structure calculations reveal that GdPtBi and NdPtBi develop Weyl points in the presence of an external magnetic field that arises from an exchange field. Our observations open the path to the realization of the quantum AHE in antiferromagnetic Heusler thin films.**

Author contributions: C.S., S.S.P.P., and C.F. designed research; C.S., N.K., V.G., S.S., R.S., H.L., S.-C.W., Y.Z., A.C.K., E.K., Y.S., J.W., W.S., A.M., U.Z., J.K., B.Y., and H.-H.K. performed research; C.S., V.G., R.S., H.L., S.-C.W., Y.Z., E.K., Y.S., J.W., W.S., A.M., U.Z., J.K., B.Y., and H.-H.K. analyzed data; and C.S., N.K., V.G., and S.S.P.P. wrote the paper.

Reviewers: A.B., University of Waterloo; and Q.-k.X., Tsinghua University.

The authors declare no conflict of interest.

Published under the [PNAS license](#).

<sup>1</sup>To whom correspondence may be addressed. Email: stuart.parkin@mpi-halle.mpg.de or shekhar@cpfs.mpg.de.

This article contains supporting information online at [www.pnas.org/lookup/suppl/doi:10.1073/pnas.1810842115/-DCSupplemental](http://www.pnas.org/lookup/suppl/doi:10.1073/pnas.1810842115/-DCSupplemental).

Published online August 28, 2018.

**Table 1. Charge carrier density,  $n$ ; mobility,  $\mu$ ; nMR, AHC, and AHA for GdPtBi and NdPtBi crystals at 2 K**

Crystal	$n, \text{cm}^{-3} \times 10^{18}$	$\mu, \text{cm}^2 \cdot \text{V}^{-1} \cdot \text{s}^{-1}$	nMR, %	AHC, $\Omega^{-1} \cdot \text{cm}^{-1}$	AHA
GdPtBi-1	1.1	3,360	63	60	0.23
GdPtBi-2	2.7	3,300	28	38	0.16
NdPtBi	0.8	1,500	20	14	0.05

nonmagnetic and we do not expect such band splitting but most of the other lanthanides gives rise to magnetism. For example, GdPtBi and NdPtBi exhibit magnetism arising from their  $4f$  electrons preserving the  $\Gamma_8$ - $\Gamma_6$  band inversion. The magnetic structures of these compounds are different: GdPtBi is a type-II antiferromagnet (18, 19) whereas the magnetic structure of NdPtBi is of type I (20). Additionally, one should note that the magnetic moments and  $f$ -level fillings are distinct for neodymium and gadolinium and the exchange field is sufficiently large to reveal, for example, four pairs of Weyl points that appear in GdPtBi when  $B \parallel [111]$  (Fig. 1D). Interestingly, an nMR was reported for GdPtBi (14) when a magnetic field  $B$  was applied parallel to the current direction. This was attributed to a chiral anomaly associated with a WSM. However, the existence of Weyl points was attributed to an external magnetic-field-induced Zeeman splitting.

The crystals studied here have been extensively investigated, as shown by X-ray diffraction, temperature-dependent resistivity, charge-carrier density, mobility, and specific heat (SI Appendix, Figs. S5–S7). Both GdPtBi and NdPtBi exhibit AFM-semimetallic behaviors with low charge-carrier densities and high mobilities, similar to that reported in ref. 22.

We have carried out extensive measurements of the field-dependent Hall resistivity  $\rho_{yx}$  and longitudinal resistivity  $\rho_{xx}$  at various temperatures for the well-oriented crystal GdPtBi-1. At a constant value of  $\theta = 0^\circ$  ( $I \perp B$ ), where  $\theta$  is the angle between the magnetic field and current directions, we find that  $\rho_{yx}$  reveals a small hump (marked region) around 2 T (Fig. 2A) at low temperatures. In  $\rho_{xx}$ , this anomaly is reflected as a pronounced dip at the same magnetic field, as can be clearly seen in Fig. 2B. This feature shifts to slightly higher magnetic fields as the temperature is increased. These anomalies in  $\rho_{yx}$  and  $\rho_{xx}$  almost disappear for  $T \geq 60$  K. Consequently, the calculated Hall conductivity  $\sigma_{xy}$  (Fig. 2C) also exhibits a peak in the same  $H$ - $T$  regime. This anomaly in  $\rho_{yx}$  is attributed to the anomalous Hall effect (AHE) which is usually observed in ferromagnetic materials (23). Recently, it has been shown that noncollinear antiferromagnets with zero net magnetization can produce a large AHE when their electronic structure exhibits a nonvanishing Berry curvature (that acts like a large fictitious magnetic field) (24–27). Zero-field (ZF)  $\mu$ SR data are consistent with collinear AFM order below  $T_N \sim 9$  K (see below). The AHE persists well above  $T_N$ , where the presence of static magnetic correlations is excluded by our  $\mu$ SR experiments. Theoretical studies have predicted that a large AHE can also be realized in Weyl semimetals that exhibit a chiral anomaly, where the anomalous Hall conductance (AHC) is proportional to the separation between the Weyl nodes (7). As discussed, GdPtBi is an ideal Weyl semimetal with field-induced Weyl nodes near the  $E_F$  (Fig. 1) and therefore exhibits an nMR when  $\theta = 90^\circ$  ( $I \parallel B$ ) (SI Appendix, Fig. S9). The AHC for GdPtBi-1 and NdPtBi at 2 K are  $60 \Omega^{-1} \cdot \text{cm}^{-1}$  and  $14 \Omega^{-1} \cdot \text{cm}^{-1}$ , respectively. Similar results given in Table 1 were obtained on a second crystal GdPtBi-2. Our findings clearly suggest a major role of the Weyl points in the AHE in GdPtBi and NdPtBi.

To investigate the AFM ordered state at low temperatures from the local point of view and examine the presence of magnetic correlations in the paramagnetic state, we have performed ZF- $\mu$ SR experiments on GdPtBi single crystals. Below  $T_N \sim 9$  K, we observe clear oscillations in the time domain of the ZF spectra as shown in SI Appendix, Fig. S14. This demonstrates a well-defined

static internal field at the muon site due to the static ordered moment of Gd spins. The frequency of the oscillations is given by the internal field at the muon stopping site, which is related to the AFM order parameter. The temperature dependence of the internal field follows the predictions for a conventional Heisenberg AFM state with a spin-wave contribution at low temperatures (Fig. 3A) (28). The amplitude of the oscillations is isotropic for two orthogonal components of the muon spin polarization (Fig. 3A, Inset). The absolute value of the amplitude is about 60% of the total asymmetry, indicating that the internal fields at the muon stopping site have an angle of about  $50^\circ$  with respect to the muon spin polarization. This is consistent with the AFM structure proposed previously (18, 19). The muon spin-depolarization rate  $\lambda_L$  (obtained from the fit of the ZF- $\mu$ SR time spectra as shown in SI Appendix, Fig. S14B), which is a measure of the fluctuations/correlations of the spins, does not show any noticeable divergent behavior across  $T_N$  (Fig. 3B). Further, in the paramagnetic state above  $T_N$ ,  $\lambda_L$  is temperature independent and isotropic for two orthogonal components of the muon spin polarization. The overall behavior suggests the absence of any significant magnetic correlations in GdPtBi above  $T_N$ .

Now we focus on the magnitude of the nMR. We investigate the evolution of the nMR with angle  $\theta$  as a function of temperature. SI Appendix, Fig. S9 shows the field dependence of  $\rho_{xx}$  at various  $\theta$  at 2 K. A large nMR is observed for  $\theta \geq 60^\circ$  and a positive magnetoresistance appears which gradually increases as  $\theta$  becomes less than  $60^\circ$ . For  $\theta = 90^\circ$ , the observed values of  $\rho_{xx}$  at 0 and 9 T are 2.1 and 0.72 m $\Omega$  cm, respectively, that gives an MR of  $-66\%$ . To explore the range of temperatures over which the nMR is found, we measured the field dependence of  $\rho_{xx}$  at different temperatures for  $\theta = 90^\circ$ . As shown in Fig. 4A,  $\rho_{xx}$  vs.  $B$  which can be divided into three regimes: (i) a moderate temperature dependence on temperature up to 12 K, (ii) an increase of  $\rho_{xx}$  with increasing the temperature up to 60 K, and (iii) a positive magnetoresistance

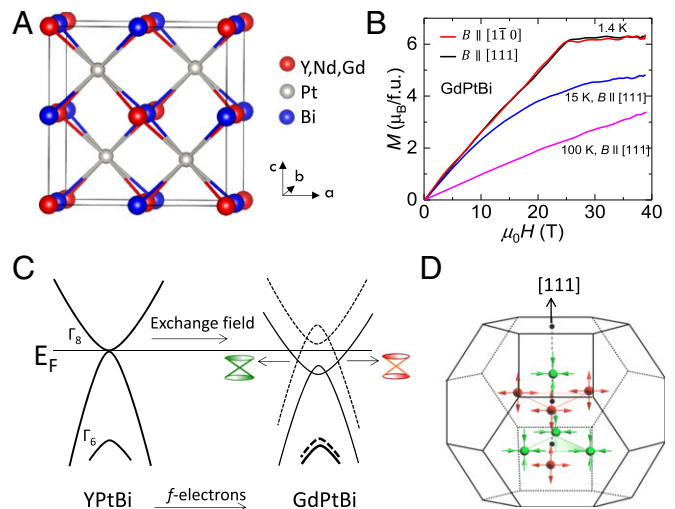


**Fig. 1. Structure, magnetization and evolution of Weyl points.** (A) Structure of cubic unit cell of RPtBi ( $R = \text{Y, Gd or Nd}$ ), (B) Magnetization in pulsed magnetic fields up to 40 T for GdPtBi at different temperature for  $B$  parallel to  $[111]$  and  $[110]$ . At  $T = 1.4$  K, the magnetization saturates at  $\sim 25$  T with a magnetic moment per Gd of almost  $6.5 \mu_B$  and magnetization is independent of crystallographic directions. (C) Schematic comparison of the calculated band structures of YPtBi and GdPtBi. The exchange field from the rare-earth elements moments lifts the spin degeneracy of the  $\Gamma_8$  and  $\Gamma_6$  bands and induces Weyl points: the green and red hourglasses represent Weyl cones with opposite chirality. (D) Distribution of Weyl points in the first Brillouin zone of GdPtBi when the magnetic moments are along  $[111]$  taken as an example. Green and red spheres represent “-” and “+” chirality, and the arrows are the Berry-curvature vectors.

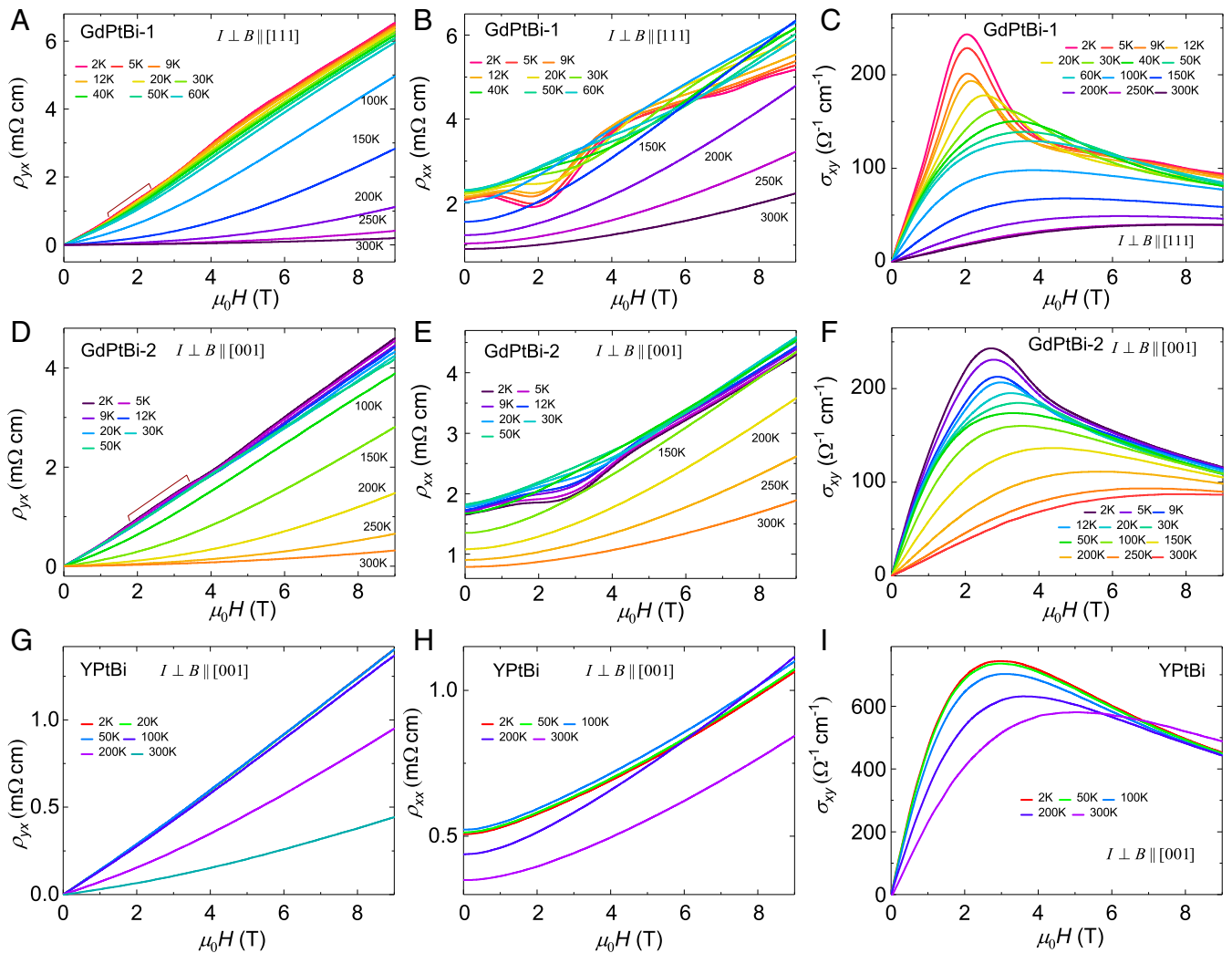


**Fig. 2.** Magnetic field dependence of resistivity at various temperatures. (A, D, and G) Hall resistivity ( $\rho_{yx}$ ); (B, E, and H) resistivity ( $\rho_{xx}$ ); and (C, F, and I) corresponding derived Hall conductivities ( $\sigma_{xy}$ ). Upper two and lower panels are for GdPtBi and YPtBi compounds, respectively, where  $\sigma_{xy}$  is calculated from the relation  $\sigma_{xy} = \rho_{yx}/(\rho_{yx}^2 + \rho_{xx}^2)$ .

above  $\sim 60$  K. An nMR below 100 K persists up to 33 T (above the saturation field of 25 T) as shown in *SI Appendix, Fig. S9*. Remarkably, the highest nMR is observed at the lowest temperature and varies only smoothly across the magnetic transition. Such MR

behavior rules out a magnetic cause and indicates the Weyl points as the origin. We have also simultaneously measured the magnetotransport properties of both NdPtBi and YPtBi. NdPtBi shows similar angular and temperature-dependent magnetotransport

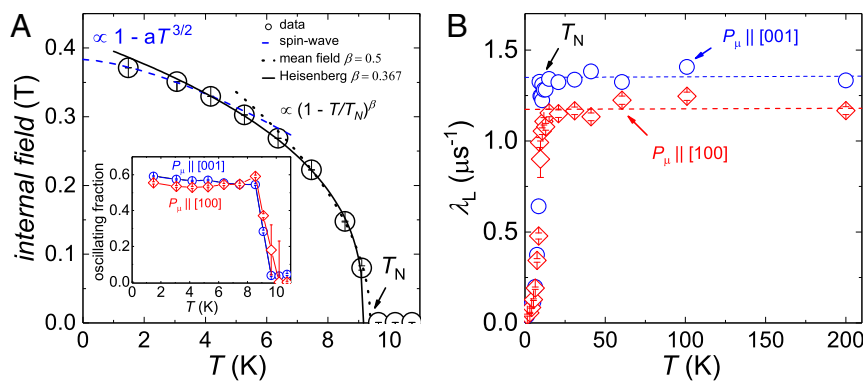


**Fig. 3.** Temperature dependence of  $\mu$ SR. (A) Temperature dependence of the internal field obtained from ZF- $\mu$ SR spectra below  $T_N$ . The overall behavior of the magnetic order parameter ( $\sim$ internal field) is consistent with a 3D isotropic AFM state. (Inset) Temperature dependence of the amplitude of the oscillating signal in ZF- $\mu$ SR time spectra. (B) The temperature dependence of the longitudinal ZF relaxation rate measured for the muon spin-polarization components  $P_\mu \parallel [100]$  and  $\parallel [001]$ . The data exclude any noticeable correlations effects above  $T_N$ .

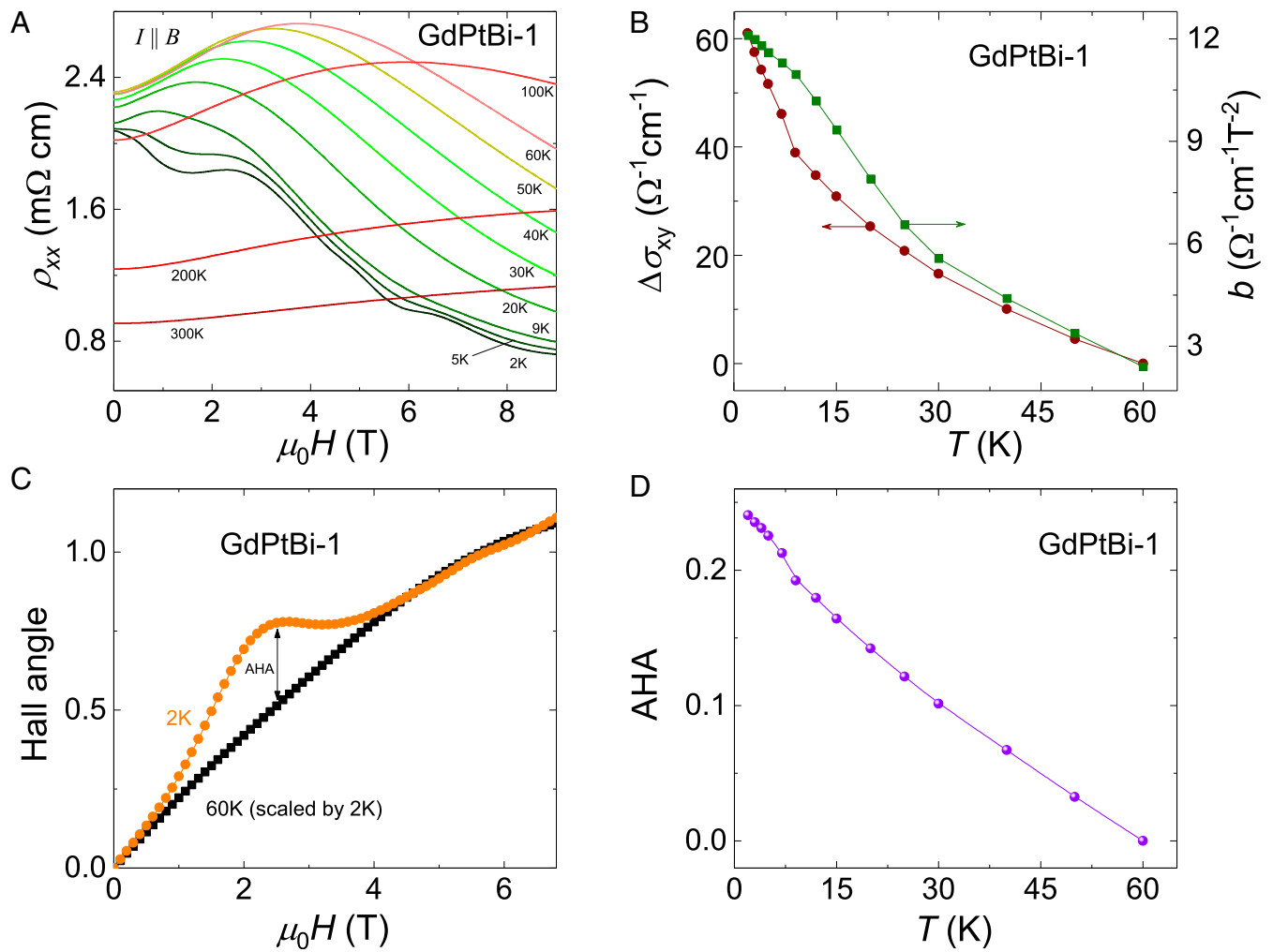


**Fig. 4.** nMR, AHC,  $\Delta\sigma_{xy}$ , and AHA,  $\sigma_{xy}/\sigma_{xx}$ . (A) nMR sustained up to 60 K in 9 T. (B) Temperature dependent AHC and coefficient of  $B^2$ ,  $b$  which is estimated by fitting the data of A with  $\sigma_{xx} = \sigma_0 + bB^2$ , where  $\sigma_{xx} = 1/\rho_{xx}$ . (C) AHA at 2 K scaled with 60-K AHA data at 5 T and the subtracted AHA plotted against temperature in D.

properties as GdPtBi. At  $T = 2$  K NdPtBi exhibits an nMR of  $\sim -20\%$  for  $I \parallel B$  in  $B = 9$  T (SI Appendix, Fig. S12). The MR decreases with increasing temperatures. In contrast to GdPtBi and NdPtBi, YPtBi does not show any AHE or nMR for similar temperature and field ranges (Fig. 2 G–I) and SI Appendix, Fig. S9B.

In an effort to find a relation between the AHE and nMR, we have used the function  $\sigma_{xx} = \sigma_0 + bB^2$  to describe the longitudinal conductivity ( $\sigma_{xx} = 1/\rho_{xx}$ ) over a wide range of temperature and field (SI Appendix, Fig. S10, data of Fig. 4A). In this way, we obtained the coefficient  $b$  that quantifies the extent of the nMR. The temperature-dependent values of  $\Delta\sigma_{xy}$  (detailed extraction method is mentioned in SI Appendix, Fig. S8) describing the AHE and  $b$  describing the nMR are shown in Fig. 4B. An excellent correlation between the magnitudes of  $b$  and  $\Delta\sigma_{xy}$  is observed over the entire temperature range (Fig. 4B). Thus, we conclude that AHE and nMR follow a similar trend with temperature, indicating their common origin. To extract the anomalous Hall angle (AHA) from the anomalous contribution of the Hall effect, we first plot the Hall angle as a function of field at various temperatures (Fig. 4C for data at 2 K; see SI Appendix, Fig. S8 for other temperatures) and then scale them by the Hall angle data of 60 K (we assumed that there is no AHE at this temperature). The Hall angle at 2 K data exhibits a broad hump around 2 T while the Hall angle at 60 K data does not show such a hump. The difference between these two data sets gives an AHA value of 0.23 which is an extremely

large value. By applying this analysis to the Hall-angle data at different temperatures, the temperature-dependent AHA is obtained, as shown in Fig. 4D. The field-dependent AHC at a particular temperature is calculated from the AHA by multiplying by the corresponding field-dependent  $\sigma_{xx}$  (SI Appendix, Fig. S8C). Our investigation of the AHE and nMR, which persist well above the  $T_N$ , establishes a strong correlation between both quantities. In GdPtBi, for which the Weyl points lie closer to the  $E_{F_1}$ , a large nMR together with a large AHE is found. Our ab initio calculations predict that the separation of the Weyl points along the [111] axis is as large as 30% of the Brillouin zone width, guaranteeing an observable AHE and chiral-anomaly-induced nMR. From the magnetotransport and magnetization data we can draw a phase diagram (SI Appendix, Fig. S13) that shows how the various physical properties of GdPtBi depend on temperature and applied field. We sketch the regions for the nMR, positive MR, and AHE from our field- and temperature-dependent measurements.

Our studies show that GdPtBi and NdPtBi become Weyl semimetals when the exchange splitting of the  $\Gamma_8$  and  $\Gamma_6$  bands is sufficiently large to establish the Weyl nodes. This, we find, happens even for small applied fields. It is clear from our experiments that this is not caused by simple external-field-induced Zeeman splitting but rather the external field results in a significant alignment of the magnetization of the AFM structure resulting in a large exchange field. Although the magnitude of this exchange field will

increase up to the saturation field ( $\sim 25$  T at  $T = 1.4$  K), it is clear that once the exchange field is sufficiently large to establish the Weyl modes, further increases in the exchange field do not much affect the Weyl properties. We propose that the dip in resistivity and the corresponding peak in the Hall conductivity at about 2 T reflect this critical exchange value and the corresponding band-gap opening. We speculate that all magnetic rare-earth RPtBi and RAuSn ( $R = \text{Ce-Sm, Gd-Tm}$ ) compounds will show related phase diagrams. For the systems CePtBi and YbPtBi the situation might be more complicated.

## Methods

**Crystal Growth.** Single crystals of Y(Gd, Nd)PtBi were grown by a solution-growth method from a Bi flux. Freshly polished pieces of Y or (Gd or Nd), Pt, and Bi, each of purity  $>99.99\%$ , in the stoichiometric ratio (with significant excess Bi, i.e., Gd:Pt:Bi = 1:1:9) were placed in a tantalum crucible and sealed in a dry quartz ampoule under 3-mbar partial pressure of argon. The ampoule was heated at a rate of 100 K/h up to 1,473 K and left for 12 h at this temperature. For the crystal growth, the temperature was slowly reduced at a rate of 2 K/h to 873 K and the extra Bi flux was removed by decanting from the ampoule at 873 K. Typically we could obtain crystals, 1–5 mm in size, with a preferred growth orientation along [111], as confirmed by Laue diffraction. The methods we used follow closely those described in ref. 29. The composition and structure was checked by energy-dispersive X-ray analysis and Laue X-ray diffraction (SI Appendix, Fig. S5), respectively. The lattice parameters of the cubic structure are 6.65 Å for YPtBi, 6.68 Å for GdPtBi, and 6.76 Å for NdPtBi, which are consistent with previous reports (29–31).

**Magnetoresistance and Heat-Capacity Measurements.** Resistivity measurements were performed in a physical property measurement system (PPMS-9T; Quantum Design) using the AC transport with rotator option. Heat capacity was measured by a relaxation method (HC option, PPMS; Quantum Design). Samples with bar shape of different crystalline orientations were cut from large single crystals using a wire saw. The orientation of these crystals was verified by Laue X-ray diffraction measurements and their physical dimensions are (width  $\times$  thickness  $\times$  length:  $w \times d \times l$ )  $0.57 \times 0.15 \times 2.0$  mm<sup>3</sup> for GdPtBi,  $0.63 \times 0.24 \times 1.21$  mm<sup>3</sup> for NdPtBi, and  $0.85 \times 0.21 \times 1.6$  mm<sup>3</sup> for YPtBi. The linear contacts were made on the orientated crystals by silver paint and 25- $\mu\text{m}$  platinum wires. The resistivity ( $\rho_{xx}$ ) and Hall resistivity ( $\rho_{xy}$ ) were measured in 4-wires and 5-wires geometry, respectively, using a current of 1.0 mA at temperatures between 2 and 300 K and magnetic fields up to 9 T. Special attention was paid to

the mounting of the samples on the rotating puck to ensure a good parallel alignment of the current and magnetic-field direction. The Hall resistivity contributions to the longitudinal resistivity and vice versa, due to contact misalignment, were accounted for by calculating the mean resistivity of positive and negative magnetic fields. Almost symmetrical longitudinal resistivities were obtained for positive and negative magnetic fields when current and magnetic field were parallel, showing the excellent crystal and contact alignment of our samples. Otherwise, the nMR was overwhelmed by the transverse resistivities, i.e., Hall resistivity and trivial positive MR.

**$\mu\text{SR}$  Measurements.**  $\mu\text{SR}$  experiments were performed on oriented GdPtBi single crystals at the GPS instrument of the  $\pi\text{M}3$  beamline at the Paul Scherrer Institute (PSI) in Villigen, Switzerland. Fully spin-polarized, positive muons with a kinetic energy of 4.2 MeV were implanted in the sample (parallel to the crystallographic  $a$  axis [100]) where they rapidly thermalize and stop at interstitial lattice sites at a depth on the order of 100  $\mu\text{m}$ . For the  $\mu\text{SR}$  experiments we used two single crystals with the thickness  $\sim 0.5$  mm placed side by side to increase the sample area ( $\sim 15$  mm<sup>2</sup>) perpendicular to the muon beam. Using veto detectors allowed us to obtain the positron signal with a background contribution below 10% of the total signal. The measurements were performed in transversal polarization mode in which the muon spin polarization  $P_\mu$  is at 45° with respect to the muon beam (pointing toward the upward counter) and sample  $a$  axis. The data were analyzed using the musrfit software package (32).

**Density-Functional Calculations.** Density-functional theory calculations were performed using the Vienna ab initio Simulation Package (33) with the generalized gradient approximation (34) of the exchange-correlation energy. The experimentally measured lattice parameters were adopted and spin-orbit coupling was included in all calculations. For the Brillouin-zone sampling  $10 \times 10 \times 10$   $k$  meshes were used. An on-site Coulomb interaction was considered for the  $f$  electrons of Gd with  $U = 10$  eV. The band structures were projected to maximally localized Wannier functions (35). The chirality of the Weyl points was confirmed by identifying the source- or sink-type distribution of the Berry curvature.

**ACKNOWLEDGMENTS.** This work was financially supported by the ERC Advanced Grant 742068 “TOPMAT.” Part of the work was supported by Deutsche Forschungsgemeinschaft (DFG) through Grant GR 4667 (to V.G.) and through the SFB 1143. We also acknowledge support from the Dresden High Magnetic Field Laboratory at Helmholtz-Zentrum Dresden-Rossendorf and the High Field Magnet Laboratory-Radboud University/Foundation for Fundamental Research on Matter (RU/FOM), members of the European Magnetic Field Laboratory (EMFL).  $\mu\text{SR}$  experiments were performed at Swiss Muon Source, PSI, Villigen.

- Wan X, Turner AM, Vishwanath A, Savrasov SY (2011) Topological semimetal and Fermi-arc surface states in the electronic structure of pyrochlore iridates. *Phys Rev B Condens Matter Mater Phys* 83:205101.
- Weng H, Fang C, Fang Z, Bernevig BA, Dai X (2015) Weyl semimetal phase in non-centrosymmetric transition-metal monophosphides. *Phys Rev X* 5:011029.
- Huang S-M, et al. (2015) A Weyl Fermion semimetal with surface Fermi arcs in the transition metal monopnictide TaAs class. *Nat Commun* 6:7373.
- Liu ZK, et al. (2016) Evolution of the Fermi surface of Weyl semimetals in the transition metal pnictide family. *Nat Mater* 15:27–31.
- Xu S-Y, et al. (2015) Discovery of a Weyl fermion state with Fermi arcs in niobium arsenide. *Nat Phys* 11:748–754.
- Kim H-J, et al. (2013) Dirac versus Weyl fermions in topological insulators: Adler-Bell-Jackiw anomaly in transport phenomena. *Phys Rev Lett* 111:246603.
- Burkov AA (2014) Anomalous Hall effect in Weyl metals. *Phys Rev Lett* 113:187202.
- Liang T, et al. (2018) Anomalous Hall effect in ZrTe<sub>5</sub>. *Nat Phys* 14:451–455.
- Chadov S, et al. (2010) Tunable multifunctional topological insulators in ternary Heusler compounds. *Nat Mater* 9:541–545.
- Lin H, et al. (2010) Half-Heusler ternary compounds as new multifunctional experimental platforms for topological quantum phenomena. *Nat Mater* 9:546–549.
- Xiao D, et al. (2010) Half-Heusler compounds as a new class of three-dimensional topological insulators. *Phys Rev Lett* 105:096404.
- Nakajima Y, et al. (2015) Topological RPdBi half-Heusler semimetals: A new family of noncentrosymmetric magnetic superconductors. *Sci Adv* 1:e1500242.
- Liu ZK, et al. (2016) Observation of unusual topological surface states in half-Heusler compounds LnPtBi (Ln=Lu, Y). *Nat Commun* 7:12924.
- Hirschberger M, et al. (2016) The chiral anomaly and thermopower of Weyl fermions in the half-Heusler GdPtBi. *Nat Mater* 15:1161–1165.
- Kumar N, Guin SN, Felser C, Shekhar C (2018) Planar Hall effect in the Weyl semimetal GdPtBi. *Phys Rev B* 98:041103.
- Hütt F, et al. (2018) Strong optical evidence of 3D linear electronic bands in GdPtBi in zero magnetic field. arXiv:1803.00840.
- Yang H, et al. (2017) Prediction of triple point fermions in simple half-Heusler topological insulators. *Phys Rev Lett* 119:136401.
- Kreyssig A, et al. (2011) Magnetic order in GdBiPt studied by x-ray resonant magnetic scattering. *Phys Rev B Condens Matter Mater Phys* 84:220408.
- Müller RA, et al. (2014) Magnetic structure of GdBiPt: A candidate antiferromagnetic topological insulator. *Phys Rev B Condens Matter Mater Phys* 90:041109.
- Müller RA, et al. (2015) Magnetic structure of the antiferromagnetic half-Heusler compound NdBiPt. *Phys Rev B Condens Matter Mater Phys* 92:184432.
- Suzuki T, et al. (2016) Large anomalous Hall effect in a half-Heusler antiferromagnet. *Nat Phys* 12:1119–1123.
- Mun E, Bud'ko SL, Canfield PC (2016) Robust tunability of magnetoresistance in half-Heusler RPtBi ( $R = \text{Gd, Dy, Tm, and Lu}$ ) compounds. *Phys Rev B* 93:115134.
- Nagaosa N, Sinova J, Onoda S, MacDonald AH, Ong NP (2010) Anomalous Hall effect. *Rev Mod Phys* 82:1539–1592.
- Kübler J, Felser C (2014) Non-collinear antiferromagnets and the anomalous Hall effect. *Europhys Lett* 108:67001.
- Chen H, Niu Q, MacDonald AH (2014) Anomalous Hall effect arising from noncollinear antiferromagnetism. *Phys Rev Lett* 112:017205.
- Nakatsuji S, Kiyohara N, Higo T (2015) Large anomalous Hall effect in a non-collinear antiferromagnet at room temperature. *Nature* 527:212–215.
- Nayak AK, et al. (2016) Large anomalous Hall effect driven by a nonvanishing Berry curvature in the noncollinear antiferromagnet Mn<sub>3</sub>Ge. *Sci Adv* 2:e1501870.
- Blundell S (2001) *Magnetism in Condensed Matter* (Oxford Univ Press, Oxford).
- Canfield PC, et al. (1991) Magnetism and heavy fermion-like behavior in the RBiPt series. *J Appl Phys* 70:5800–5802.
- Butch NP, Syers P, Kirshenbaum K, Hope AP, Paglione J (2011) Superconductivity in the topological semimetal YPtBi. *Phys Rev B Condens Matter Mater Phys* 84:220504.
- Morelli DT, Canfield PC, Drymiotis P (1996) Low-temperature transport properties of NdBiPt. *Phys Rev B Condens Matter* 53:12896–12901.
- Suter A, Wojek B (2012) Musrfit: A free platform-independent framework for  $\mu\text{SR}$  data analysis. *Phys Procedia* 30:69–73.
- Kresse G, Furthmüller J (1996) Efficient iterative schemes for *ab initio* total-energy calculations using a plane-wave basis set. *Phys Rev B Condens Matter* 54:11169–11186.
- Perdew JP, Burke K, Ernzerhof M (1996) Generalized gradient approximation made simple. *Phys Rev Lett* 77:3865–3868.
- Mostofi AA, et al. (2008) wannier90: A tool for obtaining maximally-localised Wannier functions. *Comput Phys Commun* 178:685–699.